Effects of machining methods on uniaxial tensile properties of 75μm thick 304L stainless steel foil

Lin Wang
Department of Civil Engineering, Hefei University, China
Anhui Provincial Key Laboratory of Urban Rail Transit Safety and Emergency Management, Hefei University, China
linw@smu.edu, http://orcid.org/0000-0002-6481-2409

Feng Gao
Department of Civil Engineering, Hefei University, China
1570670405@qq.com

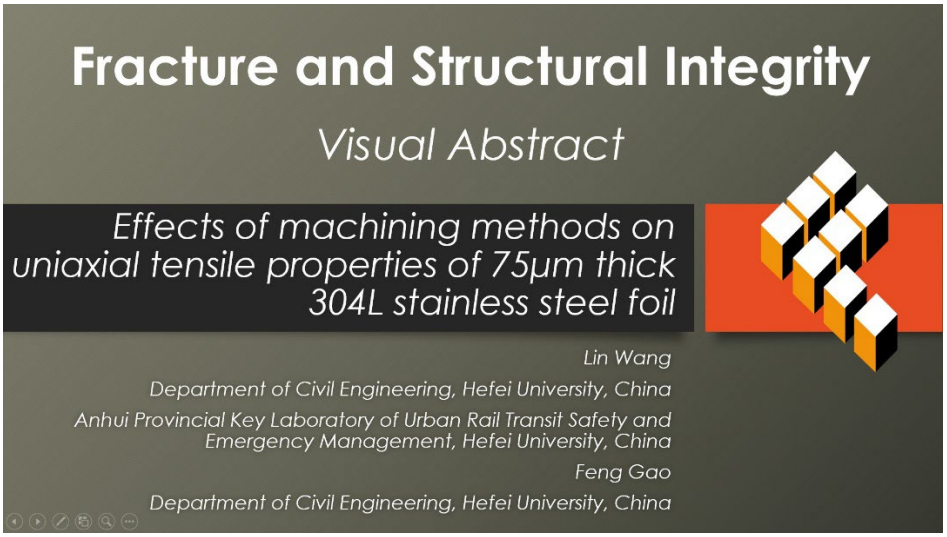

Citation: Wang, L., Gao, F., Effects of machining methods on plastic performance of 75μm thick 304L stainless steel foil under uniaxial tension, Fracture and Structural integrity, 76 (2026) 169-182.

Received: 05.12.2025
Accepted: 04.02.2026
Published: 13.02.2026
Issue: 04.2026

KEYWORDS. 304L stainless steel foil, Machining methods, Edge defect, Digital image correlation, Failure mode.

INTRODUCTION

Ultra-thin metal foil, such as the stainless steel 304L (SS304L), is promising for applications like bipolar plates in automotive fuel cells, due to their unique combination of high strength-to-weight ratio, flexibility, and conductivity [1-8]. To improve material specifications and manufacturing processes for these components, more consistent and precise data on their plastic deformation behavior and a deeper understanding of their forming failure are required. When characteristic dimensions scale down to micro-level, typically less than 300μm, materials can no longer be treated as a

homogeneous continuum. The so-called size effects phenomena emerge, causing mechanical behaviors to deviate significantly from macroscopic performance [6-8]. For ultra-thin foils, the mechanical response is primarily governed by the ratio of specimen thickness to average grain size [6-8].

Xu et al. observed that yield strength of SUS304 increases as foil thickness decreases or phenomenon as thinner is stronger due to strain gradient plasticity [9]. However, the post-yield work-hardening rate decreases. This is explained by the surface layer model [9-11]. Surface grain provides less constraint than internal grains. Consequently, the material satisfies the Considère criterion at lower strain levels, thereby reducing uniform elongation. Furthermore, SS304L exhibits unique deformation mechanisms due to transformation induced plasticity, where stable austenite transforms into martensite during straining. In micro-scale foils, such phase transformation is highly sensitive to the stress state and geometric constraints. Meng et al. demonstrated that localized transformation significantly changes strain hardening behavior compared to bulk polycrystalline material [12]. Fracture analysis indicates a fundamental change in failure mechanisms. Failure of macroscopic stainless steel is typically governed by void nucleation and coalescence, resulting in a dimpled fracture surface. In contrast, Fu and Chan reported that ultra-thin foils often fail via shear separation. The limited number of grains across the thickness prevent the formation of the triaxial stress state necessary for void growth. The failure of ultra-thin foils occurs via crystallographic slip along specific shear bands [7, 9]. As the number of grains in the cross-section decreases, the mechanical response of foil specimen is dominated by the crystallographic orientation of individual grains rather than the random texture of bulk materials. This results in significant scatter in flow stress and forming limits [8]. Understanding these intrinsic size effects is a prerequisite to identify the extrinsic influence of manufacturing processes on component reliability [6, 13].

Given their fragility, the machining processes used to fabricate such mechanical components from ultra-thin foils inevitably introduce unique signature which may affect their in-service mechanical performance. The five distinct machining methods employed in this study for sample preparation include electrical discharge machining (EDM), laser cutting, mechanical milling, waterjet cutting and photochemical etching. These processes create different edge characteristics. The EDM and laser cutting thermal processing use intense, localized heat energy to melt and vaporize material. The rapid heating and cooling create thermal stresses and microstructural change within heat-affected zone (HAZ) and recast layers [3, 4, 14-16]. The mechanical processing as milling and waterjet cutting remove undesired material by shear and high-velocity erosion, and thus induce severe work hardening and residual stress [17-19]. The photochemical etching removes material by controlled chemical dissolution, known as to produce a nearly stress-free state [20-22]. The undesired edge signatures caused by machining methods include surface roughness [3, 4, 14-19, 23-25], presence of micro-cracks or burrs [3, 4, 16, 17, 25, 27], microstructural changes caused by thermal history [3, 4, 23], grain refinement [3, 4, 18-20, 23, 24], severe work hardening [4, 17-19, 24,27] and high residual stress [4, 14]. A question naturally arises as to whether these edge signatures affect the plastic properties of the fabricated components. Recent studies on thin metal foils reveal that machining-introduced damage can dominate the failure under loading of such foils, with surface defects leading to premature fracture before the onset of macroscopic necking [17, 19, 23-29]. Such defect-driven failure hinders the accurate measurement of intrinsic material properties. While the machining effects are well-documented for thick sheets, their influence on the tensile properties of ultra-thin stainless-steel foil remains poorly understood.

Although extensive research on size effects of SS304L foils, there are still critical gaps remaining. The interaction between machining-induced edge signatures and gage width on uniaxial tensile properties of 75μm thick SS304L specimen remains unclear. In the meantime, if the machining-induced edge damage overrides intrinsic material stability to dictate failure initiation is not yet quantified across multiple manufacturing processes. This study aims to address these gaps by evaluating five distinct machining methods across four gage widths on material strength, ductility, and failure mode. The novelty of this work is by integrating of full-field digital image correlation (DIC) to provide a comprehensive understanding of how machining induced signatures interact with geometric size effect. This allows us to distinguish between defect-driven and necking-driven failure, providing new insights into the coupled effects of fabrication signatures and geometric size effects on the uniaxial tensile performance of SS304L foils.

MATERIAL AND METHODS

Material characterization

The 75μm thick cold-rolled stainless-steel foils SS304L was supplied by General Motors R&D Center. It is a face-centered cubic material. The nominal chemical composition is detailed in Tab. 1. The as-received foil surface (rolling × transverse or RD×TD plane) was observed using a Keyence VHX-500 optical microscope and a scanning electron microscope. Both optical and secondary scattered electron (SE) images show distinct rolling marks along the rolling direction of as-received foil, as shown in Fig.1a and Fig.1b. The average spacing of these marks is approximately 25μm. The

surface roughness measured by a Nanovea PS50 non-contact optical profilometer is around 1μm. Electron backscatter diffraction (EBSD) was used to characterize the microstructure. The EBSD processing parameters included an accelerating voltage of 20.00 kV and a step size of 0.5μm.

Cr	Mn	Si	Ni	P	C	S	Fe
18	≤2	≤0.75	8.9	≤0.04	≤0.03	≤0.015	balanced

Table 1: Nominal compositions of SS314L stainless-steel foils.

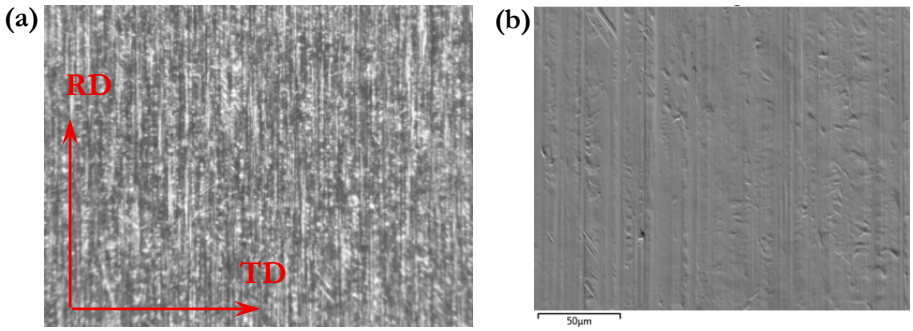

Figure 1: (a) Surface images of SS304L foil by optical microscope (1.8mm×1.35mm) and (b) scanning electron microscope.

Fig.2(a) shows the EBSD map of the as-received SS304L foil in the RD×TD plane. The grains are mostly equiaxed with extensive twinning within the grains. The average grain size is 3.76μm if considering twins or 7.13μm if disregarding twins. Based on the 75μm foil thickness, there are only 7 to 12 grains on average through the thickness. The inverse pole figures (IPF) in Fig.2(b) confirms that the SS304L foil has an almost random micro-texture.

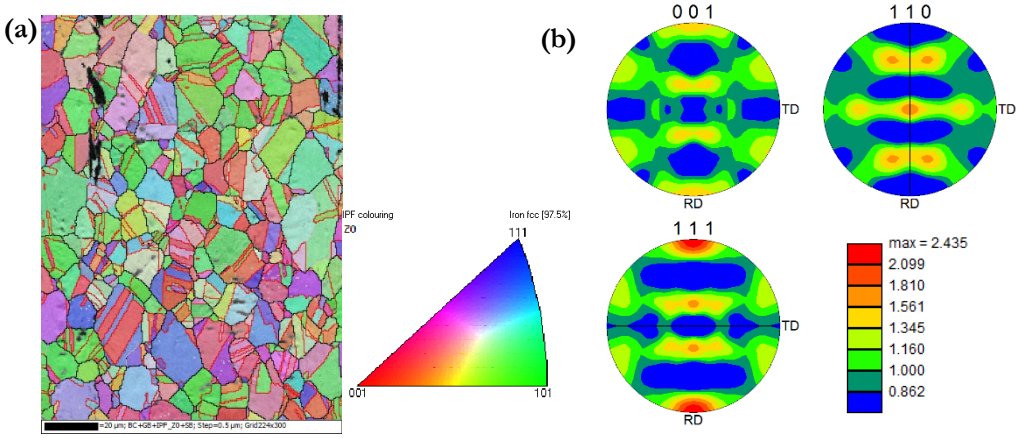

Figure 2: Microstructure of SS304L foil in (a) EBSD and (b) inverse pole figure maps.

Specimen manufacturing

Dog-bone tensile specimen with four different gage widths were fabricated, as shown in Fig.3. The specimens were manufactured using five different methods, namely, EDM, laser-cutting (LC), mechanical milling (MM), photochemical etching (PE) and water-jet cutting (WJC). The axial loading direction for all specimens was aligned with the rolling direction of foils. The wire EDM process works by creating an electrical discharge between a wire electrode and a stack of thin foil pieces. A Charmilles Robofil wire EDM machine was used feeding a zinc-coated brass wire of 0.25mm±0.01mm in diameter and a cutting speed was about 0.075mm/s. The laser cutting process used a CNC-controlled laser beam moving along the predefined specimen geometry on the SS304L foil sheet. The samples were cut with a modulated 100W fiber laser, which had a beam diameter of 20μm and a traveling speed of 25 mm/sec. For mechanical milling method, SS304L foil sheets (15mm wide, 70mm long) were first sandwiched between two aluminum plates that had the same geometry as the tensile specimen. This assembly was clamped, and one side was milled using a CNC machine. After one side was finished, the assembly was rotated and re-clamped to mill the other side. In photochemical etching process, the CAD image of specimen

was first laser plotted onto the foil sheet with a resolution less than 10μm. A photoresist coating was then bonded to the foil sheet. A acid etchant was sprayed on both surfaces simultaneously to etch the unwanted material. The photoresist was removed using an alkaline wash to obtain the final specimen. This process achieved a nominal dimensional tolerance of ±0.025 mm. The micro water–jet machining of the SS314L tensile specimens used a mix of fine abrasive and accelerated water. The average impact speed was approximately 800m/s. The stated cutting for this technique was ±0.01mm, and the positioning accuracy was ±0.003mm.

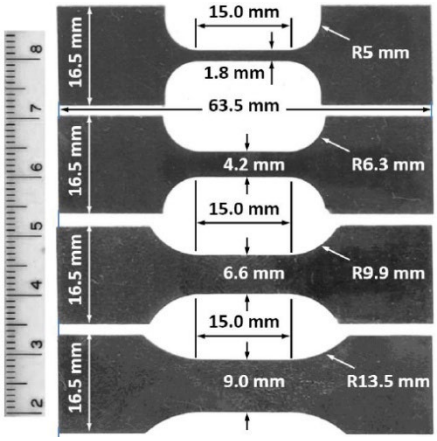

Figure 3: Geometry of the SS304L tensile specimen.

Edge roughness characterization

After manufacturing, the dimensional irregularities and edge damage of the tensile specimens were characterized. Given the fragility of the ultra-thin foils, a non-contact, image -based method was adopted. To quantify the edge roughness, specimens with a 6.6mm gage width were selected from each of the five machining processes. Both edges of the entire 15mm gage section was continuously imaged using a Keyence VHX-500 optical microscope at 200× magnification (0.96μm/pixel). Edge profiles were extracted using a MATLAB based image processing algorithm. The edge profile was defined by the y-coordinate of the edge pixels after correcting for global slope. Based on the acquired digital images, the measured error for the edge profile was estimated to be less than 0.5μm [30]. The two-dimensional edge profile was assumed to be identical through the specimen thickness. The root-mean-square roughness Rq was then calculated from the profiles of both edges over the entire gage length.

Tensile testing

Uniaxial tensile tests were performed on the 75μm thick SS304L foil specimens using an Instron E1000 testing machine (±1000N load capacity, ±0.1N accuracy), as shown in Fig.4. Tests were conducted at a controlled crosshead speed, resulting in a constant nominal strain rate of 1×10^{-3}/s. A small preload resulting in approximately 30 MPa of axial engineering stress was imposed to ensure the specimen surface was flat for image capture. Before testing, a speckle pattern of fine black-to-white paint droplets was sprayed onto one surface of the specimen to facilitate the digital image correlation (DIC) based surface strain measurement technique. During the test, a CCD camera continuously captured the high-contrast images of specimen surface at 3 frames/sec. The captured images (1280×960 pixels, 8-bit gray scale) were processed using the open-source two-dimensional DIC MATLAB code Ncorr [21]. A subset radius of 20 pixels and a grid spacing of 2 pixels were used for the DIC processing. Based on the captured reference images of tensile specimen before the test, the measurement error in axial strain is estimated to be less than 0.5μm.

The axial engineering and true strain based on the DIC measured axial elongation D over the interested initial gage length L_0 were calculated as

$$\varepsilon_e = D / L_0, \varepsilon_t = \ln(1+\varepsilon_e) \tag{1}$$

The engineering uniaxial stress was computed from

$$\sigma_e = F / A_0 \tag{2}$$

where A_0 is the original cross-section area of tensile specimen.

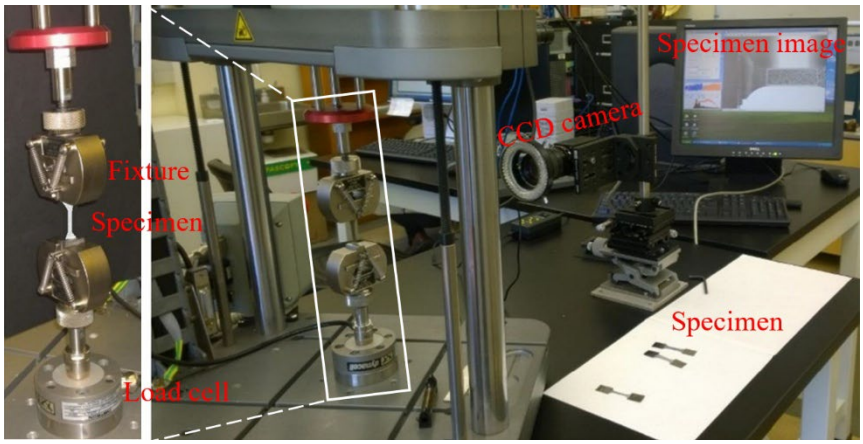

Figure 4: Setup of tensile test.

EXPERIMENTAL RESULTS

Edge morphology observation

Fig. 5 shows representative micrographs and edge profiles for specimens from each of the five machining methods. The calculated RMS edge roughness R_q is summarized in Tab. 2. The edge quality varied significantly between the methods. The EDM fabricated specimens produce the roughest edge, with R_q = 5.6±3.4μm. The edge shows an up to 50μm wide darkened thermal-affected zone and large profile fluctuations, with a peak-to-valley roughness exceeding 20μm. The water-jet cutting method produced the second-roughness R_q measured as 4.8±2.6μm. The micrographs show an abrasive-scarred edge, which is typical for high-velocity abrasive slurry impingement. The laser cutting and photochemical etching processes had intermediate roughness, 2.3±1.3μm and 2.0±1.4, respectively. The laser cutting specimen had a general smooth edge with a narrow-darkened zone approximately 10 to 20μm wide and some solidification melt spots. The photochemical etched specimen had clean edges with a morphology resulting from chemical dissolution. The mechanical milling produced the smoothest edge, with R_q = 1.7±0.8μm. The edges were very smooth and clean, with the smallest profile variation limited to ±5μm.

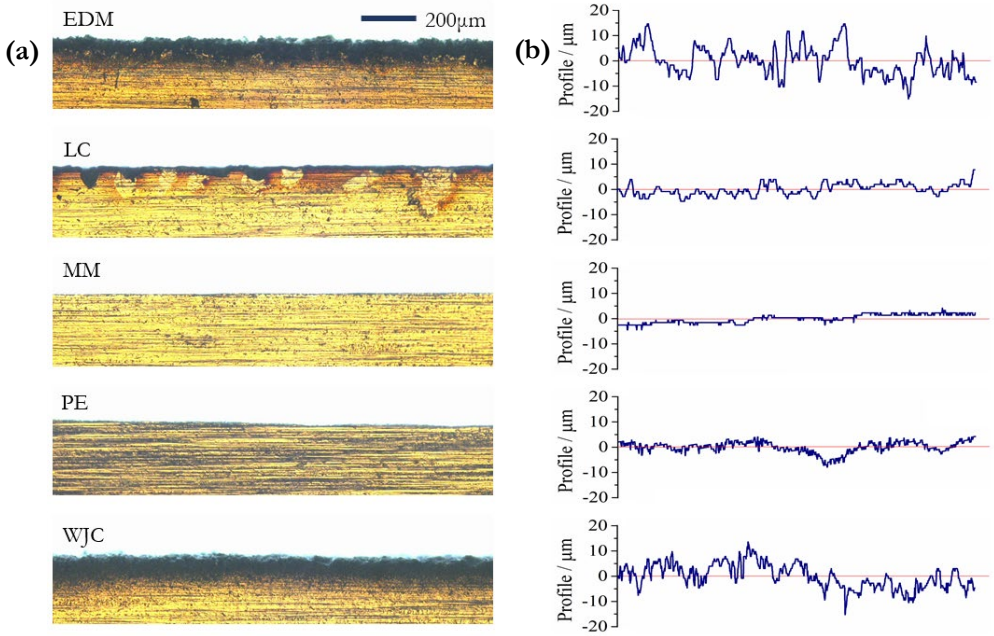

Figure 5: (a) Partial edge morphology of foils tensile specimen and (b) corresponding measured edge roughness profiles.

Machining Methods	EDM	LC	MM	PE	WJC
Edge Roughness R_q / μm	5.6±3.4	2.3±1.3	1.4±0.8	2.0±1.4	4.8±2.6

Table 2: Edge roughness of as-machined foil specimens

Uniaxial tensile properties

The engineering stress strain curves for all 40 tests are shown in Fig. 6 in the manner of averaged stress-strain relations and its corresponding variation scopes per 5 different machining methods. Fig. 6 shows all 40 tests begin to yield in a narrow range of yielding stress approximately 315-350 MPa. After yielding, the material exhibits significant strain hardening, where the stress required to continue deformation increases up to a peak, with uniform elongation around 0.43-0.78. The ultimate tensile strength (UTS) was also consistent across all tests, clustering tightly from 678 to 724 MPa. In contrast to the strength properties, the ductility shows high variability. The fracture or total elongation is spread across a wide range, from an engineering strain of approximately 0.43 to as high as 0.79. Although with significant plasticity, the post-necking deformation is only about 0.01-0.03. All measured uniaxial tensile properties of foil as 0.2% yielding stress, UTS, uniform elongation, and fracture elongation of all 40 samples from the engineering stress-strain curves are listed in Tab. 3.

Plastic deformation and failure mode

The plastic deformation of foil specimens during the tensile test was quantified using DIC-based algorithm Ncorr [21]. Tab. 4 shows the DIC measured axial true plastic strain contours over the entire gage section in deformed configuration. It presents two methods for analyzing strain localization. Cumulative strain mapping compares the final image before failure with the reference image captured just prior to yielding. The cumulative mapping defines the plastic axial strain distribution, which is used to identify strain localization and to quantify the maximum strain level before fracture. The results show that the maximum local strain of tensile specimen before fracture dependent on the machining methods of samples. The laser-cut and photochemical etched specimens achieved the highest local strain inside the gage section, ranging from 0.61 to 0.66. This maximum value of local strain approximately 0.66 before fracture can thus be considered the representative fracture strain for as-received SS304L foils. The mechanically milled specimens reached a lower maximum local strain, approximately 0.55-0.62. The EDM manufactured specimen achieved a maximum strain approximately 0.51-0.58. The maximum local strain was achieved inside the gage section for specimens prepared by aforementioned four processes. The water-jet cut specimens had the lowest maximum local strain, only 0.45-0.48. This maximum strain was located at the specimen edge.

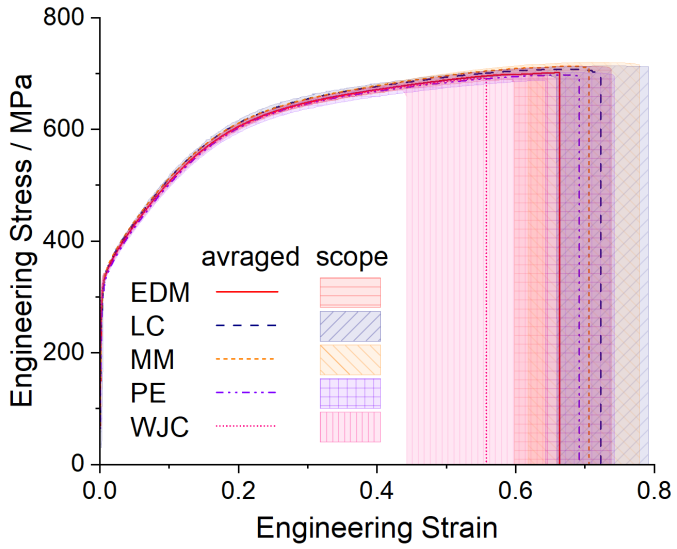

Figure 6: Averaged engineering stress-strain and its variation scope respect to 5 different machining methods.

Alternatively, incremental strain mapping compares successive image pairs to reveal the strain localization during the necking stage. For SS304L material, the strain increment between the onset of diffuse necking and the final fracture is small, typically from 0.01 to 0.03 (as detailed in Tab. 3). Therefore, the final two frames are selected to quantify the strain localization behavior. The incremental axial true plastic strain mapping in Tab. 4 indicates the location of deformation localization by

comparing the last two images just prior to final fracture, which predicts the failure initiation site. In general, such increment is within the range of 6 to 25 microns. The results showed a clear difference based on the machining method. For specimens prepared by EDM, mechanical milling, and water-jet cutting, the peak incremental strain was located at the top or bottom edge. In contrast, for laser cut and photochemical etched specimens, the peak incremental strain was located in the central part of the gage section. In all tests, the final fracture location coincides well with the location of this high incremental strain concentration.

Methods	Samples Width / mm	Yield stress / MPa	UTS / MPa	Uniform Elongation	Fracture Elongation
EDM	1.8	331.6	706.4	0.650	0.680
	1.8	322.3	688.5	0.576	0.589
	4.2	325.2	703.7	0.573	0.602
	4.2	323.5	698.4	0.589	0.595
	6.6	338.5	699.5	0.711	0.739
	6.6	328.4	705.2	0.690	0.699
	9.0	330.6	724.0	0.685	0.709
	9.0	335.4	719.3	0.685	0.698
LC	1.8	349.9	724.6	0.679	0.706
	1.8	340.5	719.8	0.682	0.711
	4.2	323.0	701.3	0.624	0.642
	4.2	341.2	708.1	0.728	0.754
	6.6	337.7	703.7	0.711	0.725
	6.6	328.3	717.3	0.687	0.704
	9.0	320.0	709.6	0.772	0.791
	9.0	341.7	698.3	0.732	0.749
MM	1.8	315.2	713.0	0.623	0.632
	1.8	339.1	708.7	0.636	0.652
	4.2	327.2	708.9	0.600	0.608
	4.2	344.2	715.3	0.735	0.768
	6.6	335.9	717.4	0.728	0.740
	6.6	326.6	712.9	0.670	0.779
	9.0	331.4	715.6	0.687	0.696
	9.0	322.5	723.0	0.740	0.770
PE	1.8	334.1	710.4	0.632	0.647
	1.8	323.6	699.5	0.631	0.644
	4.2	334.9	702.6	0.690	0.706
	4.2	338.5	705.3	0.659	0.670
	6.6	324.0	704.9	0.684	0.702
	6.6	328.8	701.6	0.682	0.697
	9.0	325.4	708.6	0.719	0.728
	9.0	330.6	696.6	0.723	0.740
WJC	1.8	327.3	697.4	0.586	0.602
	1.8	317.4	693.7	0.543	0.548
	4.2	342.5	710.9	0.631	0.645
	4.2	322.2	704.2	0.575	0.578
	6.6	333.7	706.0	0.523	0.544
	6.6	324.0	702.1	0.507	0.516
	9.0	326.0	703.3	0.576	0.593
	9.0	315.9	678.1	0.428	0.433

Table 3: Measured uniaxial tensile properties of all 40 SS304L foil tensile tests

The DIC analysis in Tab. 4 provides specific details on the failure modes. For example, the 9.0mm wide laser cut specimen shows a classic well-developed diffuse neck. The cumulative strain contour has a symmetric bullseye pattern with a maximum strain over 0.66. The incremental strain map shows this deformation localizing into a small, intense, and slightly inclined region, where the final jagged fracture path matches this localized region. This suggests that the fracture initiated in the center and propagated outwards. In comparison, the 4.2mm wide photochemical etched specimen shows an asymmetric diffuse neck, with a peak strain approximately 0.64. This asymmetry could be due to a very small imperfection in material

or sample geometry. The incremental axial strain plot reveals that the final failure occurred in a single narrow and inclined shear band formed within the larger diffuse neck. The final fracture path confirms this shear-dominated failure mode.
In contrast to the laser cut and photochemical etched samples, the water-jet cut specimens did not show a well-developed diffuse neck from the cumulative axial strain map. For the 6.6mm and 9.0mm wide specimens, the maximum axial strain achieved at the specimen edges and was only 0.47 and 0.49, respectively. The incremental deformation contour did not localize into a single shear band, but instead formed two distinct inclined shear bands in a V pattern. The distribution of cumulative and incremental strain maps indicates a premature failure occurred in water-jet cut specimens.
The 6.6mm wide specimen fabricated by mechanical milling also formed a well-developed symmetric diffuse neck. The peak value is approximately 0.65, the same as the laser cut and photochemical etch samples. The incremental strain map shows a single inclined narrow shear band, coincident with the shear-dominated failure mode. The other specimens prepared by mechanical milling and EDM achieved their peak value in cumulative or incremental strain on the top or bottom edges. These strain plots show a clear presence of strain concentration at the edges, which was likely caused by machining induced edge imperfections.

DISCUSSIONS

The five machining methods used in this work represent three distinct processing families as chemical, mechanical and thermal types. Each manufacturing method leaves a unique artifact or defect on the specimen edge, such as severe work hardening, high residual stress, or a rough edge profile. These edge defects can act as the potential weakest points of the specimen. Failure is thus likely to initiate from the most severe edge defect, which would influence the measured uniaxial tensile properties of the foil itself.

Insensitivity of strength to machining method

Fig. 7 compares the measured tensile properties of SS304L specimen from the five machining methods. Based on the one-way analysis of variance (ANOVA), the overall p-value of 0.2% yield stress is 0.233, which is much larger than the 0.05 significance level. Even for the most-different pair as laser and waterjet cutting, the p-value is approximately 0.198. For the ultimate tensile strength, the overall p-value is 0.056, slightly larger than the 0.05 level. The post-hoc test showed the p-value is approximately 0.06 for the most-different pair between mechanical milling and waterjet cutting. These statistical results indicate there is no statistical evidence that the measured yield stress or UTS is sensitive to the machining methods. The small variations in strength between groups, as shown in Fig. 7, are most likely due to normal, random experimental variation. This is consistent with the fundamental solid mechanics principles that yield stress and UTS are bulk properties, representing the average response of material across gage width. Localized edge defects, even the significant roughness from EDM and waterjet cutting, constitute only a very small fraction of the total gage volume. They do not appreciably change the effective cross-sectional area or the average stress state required to initiate and sustain global plastic flow. The remarkable consistency of the strength properties of all 40 tests also confirmed this fact. However, this finding differs from the results reported in [27].

Critical role of machining method on ductility

In contrast to the strength properties, the ductility showed high variability. The uniform elongation ranged from 0.51 to 0.77, and the fracture elongation from 0.52 to 0.79. An ANOVA analysis with a post-hoc test confirmed a statistically significant difference. The sample fabricated by the waterjet cutting had much lower uniform and total elongations than the other 4 methods.
The DIC-measured axial surface strain contours in Tab. 4 explain why the difference happened by revealing the locations of failure initiation. Specimen prepared by laser cutting and photochemical etching consistently failed within the central part of the gage section. The strain contour generally shows a classic well-developed diffused neck just prior to the final fracture. The incremental strain maps confirm a subsequent shear-dominated failure initiating from its central necked region. The failure is governed by the intrinsic plastic instability of the SS304L foil material itself, allowing the specimens to reach their maximum intrinsic ductility. Although laser cut is a thermal process that creates a hard affected zone, its edge was moderately smooth and resistant to crack initiation [33]. Unlike in other reports [25, 26], this HAZ of SS304L samples actually did not create a stress concentration large enough to trigger premature failure. The photochemical etching technique does not introduce significant thermal damage or residual stress, and thus making it suitable for preserving the intrinsic properties of materials. For both of these methods, high consistency in tensile elongation reveals that the moderate level of edge imperfection was not the weakest link and did not trigger the final failure.

Specimen Methods	Width	Cumulative true plastic strain in axial direction (mm/mm)	Incremental true plastic strain in axial direction (10^{-3} mm/mm)	Fractured Specimen
EDM	1.8mm	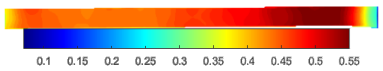	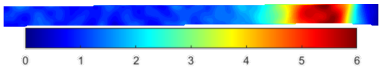	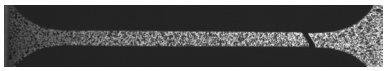
	4.2mm	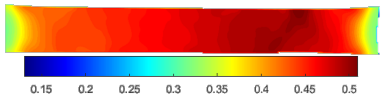	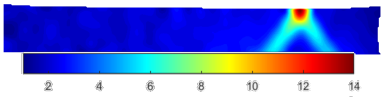	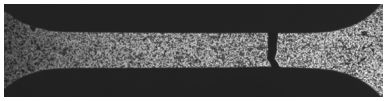
	6.6mm	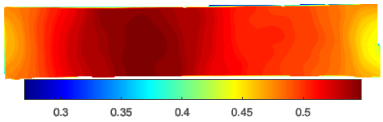	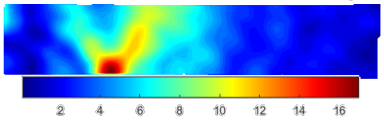	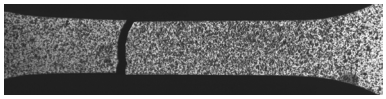
	9.0mm	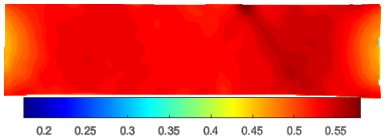	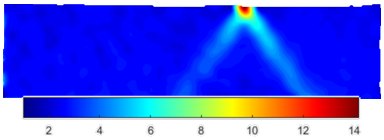	
LC	1.8mm	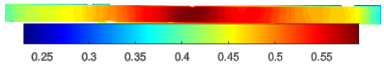	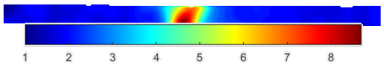	
	4.2mm	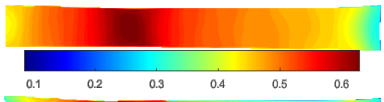	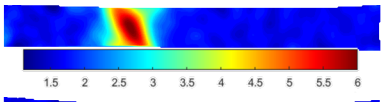	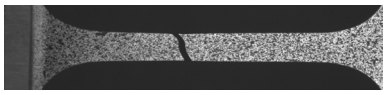
	6.6mm	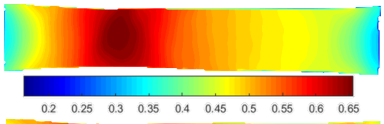	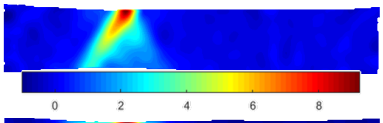	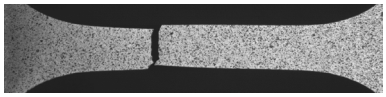
	9.0mm	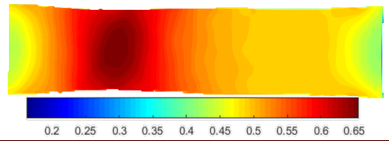	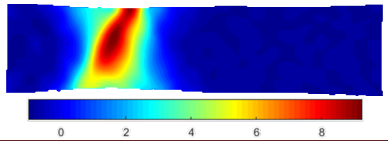	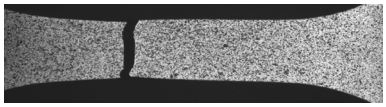
MM	1.8mm	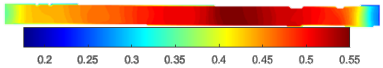	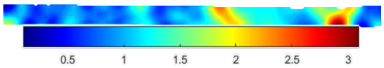	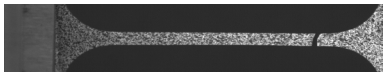
	4.2mm	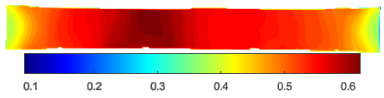	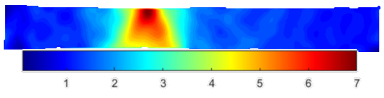	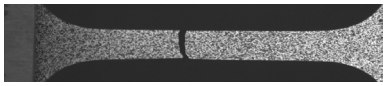
	6.6mm	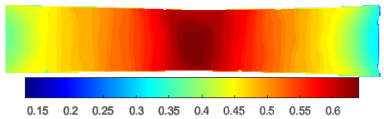	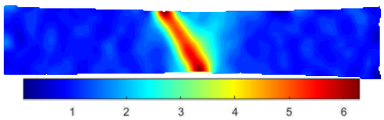	
	9.0mm	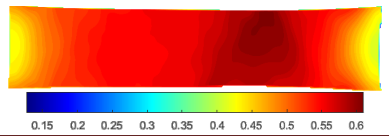	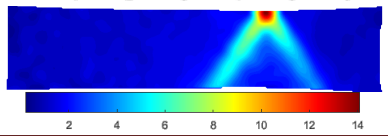	
PE	1.8mm	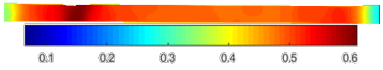	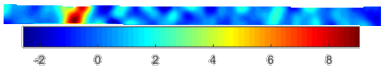	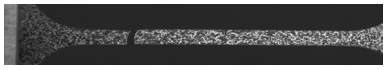
	4.2mm	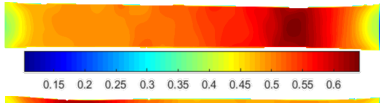	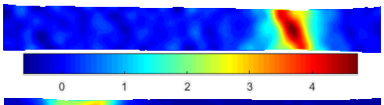	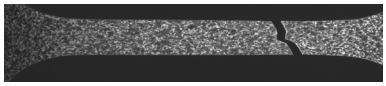
	6.6mm	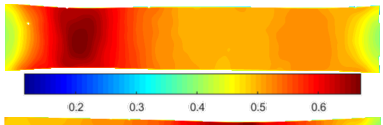	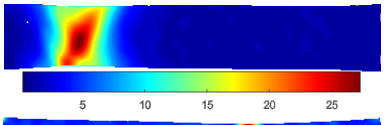	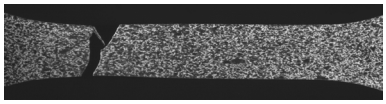
	9.0mm	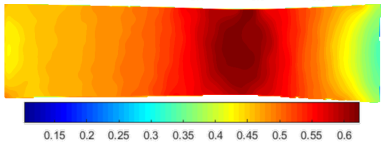	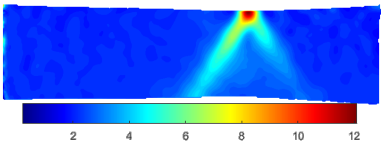	

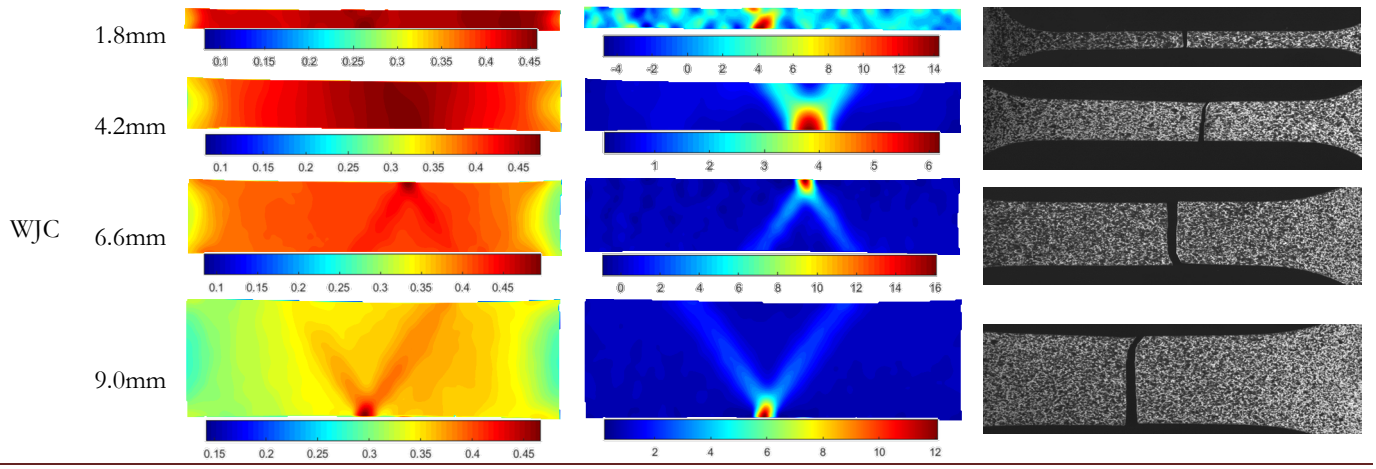

Table 4: DIC measured cumulative and incremental strain maps and failed specimens.

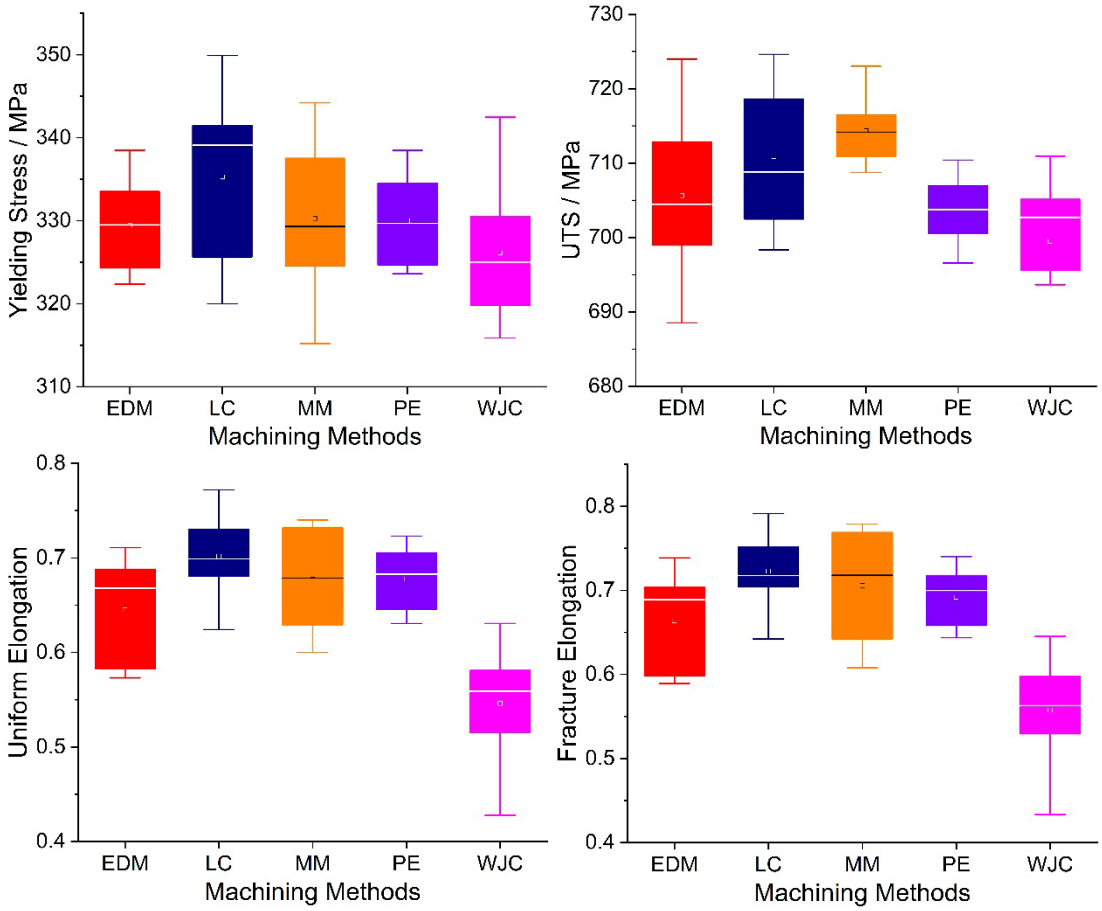

Figure 7: Statistical comparison of measured plastic properties of foil specimen fabricated by 5 machining methods

In contrast, specimens prepared by EDM and waterjet cutting predominantly failed from the specimen edges. The EDM process involves rapid melting and quenching, which creates a recast layer filled with micro-cracks and results in a rough edge profile [23, 26]. While not a thermal process, waterjet cutting also produces a rough edge finish that may contain micro-cracks [27, 28]. The EDM and waterjet cutting methods produced the highest edge roughness *Rq* of 4.8µm and 5.6µm, respectively. Under tension, these defects act as stress raiser, which concentrate stress at the sample edge and initiate failure. As a result, strain localization occurs prematurely in shear bands originating from these edge defects, preventing the formation of a fully

developed diffuse neck. The large variation in uniform and fracture elongation, as shown in Fig.7, confirms the defect-driven premature failure mechanism of samples fabricated by these two methods.

It is interesting to note that the mechanically milled specimen also failed from the specimen edge, despite having the smoothest edge profile (R_q=1.4±0.8μm). As a classic cold mechanical process, it introduces a severely work-hardened zone and possible tear burrs. The premature failure is likely caused by a combination of a local stress concentration from a burr with a relatively low-ductility material within the work-hardened zone [19].

Based on this experimental results, edge roughness R_q alone is not a sufficient metric to predict the failure mode of the ultra-thin SS304L foil. Although the mechanical milling method produced the smoothest edge profile (R_q=1.4±0.8μm), these samples still failed prematurely from the edge. This indicates that other process-induced defects, such as the severe work-hardened zone or burrs, are more critical than R_q. The failures of specimen manufactured by EDM, waterjet cutting and mechanical milling are all classic cases of defect-driven failure. In contrast, the laser cut and photochemical etched samples failed from the central portion of the gage section. This means their failure was governed by intrinsic plastic instability. Therefore, the laser cutting and photochemical etching methods are suitable for measuring the true intrinsic tensile properties of the as-received SS304L foil.

Influence of specimen gage width

Fig.8 compares the averaged tensile properties for the four distinct gage widths of the SS304L specimens fabricated by five machining methods. The 0.2% yield stress and UTS show no clear trend with respect to gage width. This is expected as strength properties reflect the average bulk response of the material. This finding for the strength is different from a previous study [19]. In contrast, the ductility as uniform and fracture elongation does show a clear size effect. For samples fabricated by the EDM, laser cutting, mechanical milling, and photochemical etching techniques, the uniform and fracture elongation increase as the gage width increases. This is consistent with other reported results [19, 25]. For instance, the fracture elongation of EDM samples increased from 0.63 at 1.8mm width to 0.70 at 9.0mm width. Similarly, the mechanically milled samples achieve a fracture elongation as 0.73 at width 9.0mm, while 0.64 with specimen width 1.8mm.

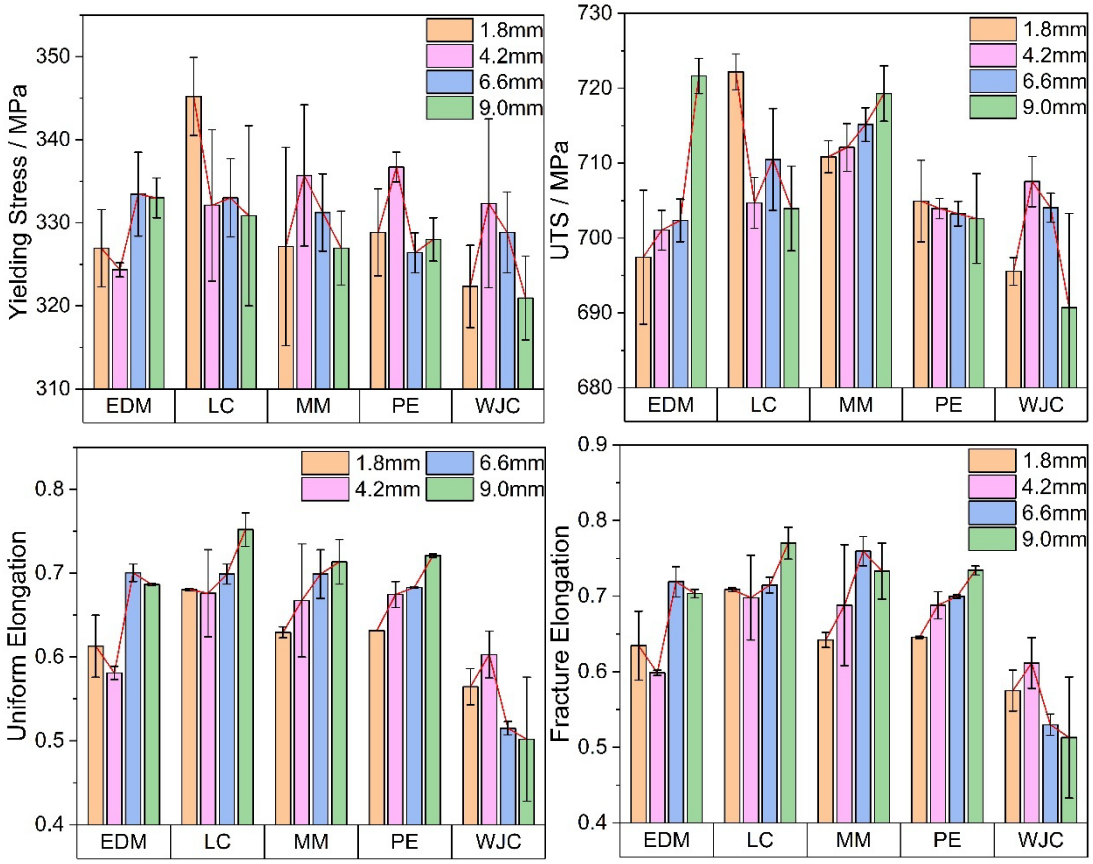

Figure 8: Comparison of tensile properties of foil specimen with different gage section width.

The experimental results show a clear size effect of specimen width on both uniform and fracture elongation. The reduction in uniform strain with decreasing width is consistent with the surface layer model [9-11, 31, 32]. Grains on surfaces of cross-section provide less constraint against plastic deformation than interior grains. As specimen width decreases, the volume fraction of these surface grains increases. This leads to a lower work-hardening rate, which satisfies the Considère criterion at earlier strain levels to the onset of diffuse neck.

Fracture strain also obviously depends on specimen width due to machining-induced edge defects. In narrower specimens, the machining-affected zone constitutes a larger portion of the total cross-section. These edge defects serve as critical stress concentrators that trigger premature fracture at relatively smaller strain level. On the other hand, wider specimens with smaller ratio of machining-affected zone to its cross-section suppress localized necking and allows for larger total deformation before failure [33-35]. For instance, the damage-free photochemical etched samples and laser cutting samples with harder HAZ edge have stable edges to resist premature failure. These stable edges allow the specimens to benefit from the geometric constraint in wider geometries, results in higher ductility. Meanwhile, a narrower specimen also has a higher ratio of edge material to bulk material, which could amplify the effect of any premature edge failure mechanism [23, 25].

The waterjet cut specimens consistently showed the lowest average ductility, which indicates obvious premature failure caused by the manufacturing. The severe edge damage, such as micro-cracks and high residual stress introduced by the high-energy abrasive process triggered this premature failure. Therefore, the ductility of samples fabricated by waterjet cutting did not increase with gage width, which were the only group to show no beneficial size effects. The EDM and mechanically milled samples showed a more complex behavior. These specimens also failed from the edge due to process-induced defects. However, they still exhibited the geometric size effect, showing a clear increase in ductility as the gage width increased. This suggests that their moderate edge damage was not severe enough to completely negate the stabilizing effect of the wider geometry, unlike the damage in the samples prepared by the waterjet cutting.

It is worth mentioning that image-based characterization of edge profiles alone is insufficient to fully quantify microstructural variations induced by machining. EBSD is suggested to provide a more detailed analysis of grain size and phase distribution after thermal history. This technique is also able to calculate dislocation densities to measure strain hardening from mechanical milling. High-resolution scanning electron microscopy should also be used to detect edge defects such as micro-cracks and burrs.

Conclusion

In this study, the effects of five different machining methods and four distinct gage widths on the uniaxial tensile properties of 75μm thick SS304L stainless steel foils were investigated. Based on the experimental results, the following key insights are drawn.

1. The 0.2% yield stress and UTS are consistent across all 40 tested specimens, since the strength represents the average response of the entire gage section, which is not significantly affected by localized edge quality and gage width.
2. Uniform and fracture elongation show obvious dependence on the fabrication process because the machining method dictated the failure mode. The laser cut and photochemical etched specimens failed by intrinsic plastic instability.
3. Specimens from the other three methods failed prematurely as a result of process-induced edge damage, which is a more critical factor for failure initiation than the edge roughness alone.
4. A size effect of specimen width was observed, but it can be negated by severe edge damage. For samples with good or moderate edge quality, the ductility clearly increased as the gage width increased. The severe edge damage from waterjet cutting dominated the defect-driven premature fracture before a stabilizing geometric effect could take place.

Acknowledges

Financial supports from the University Natural Sciences Research Program of Anhui Province (KJ2021A1001) and Academic Visit Program of Anhui Province (gxgnfx2022054) are greatly appreciated.

REFERENCE

[1] Simons, G., Weippert, C., Dual, J., Villain, J. (2006). Size effects in tensile testing of thin cold rolled and annealed Cu foils. Materials Science and Engineering: A, 416(1-2), pp. 290-299. DOI: https://doi.org/10.1016/j.msea.2005.10.060.

[2] Lederer, M., Gröger, V., Khatibi, G. and Weiss, B. (2010). Size dependency of mechanical properties of high purity aluminium foils. Materials Science and Engineering: A, 527(3), pp. 590-599. DOI: https://doi.org/10.1016/j.msea.2009.08.016.

[3] Buj-Corral, I., Costa-Herrero, L., Domínguez-Fernández, A. (2021). Effect of process parameters on the quality of laser-cut stainless steel thin plates. Metals, 11(8), 1224. DOI: https://doi.org/10.3390/met11081224.

[4] Pereira, R., Peixinho, N., Costa, S. L. (2024). A review of sheet metal forming evaluation of advanced high-strength steels (AHSS). Metals, 14(4), 394. DOI: https://doi.org/10.3390/met14040394.

[5] Bolzon, G., Shahmardani, M., Liu, R., Zappa, E. (2017). Failure analysis of thin metal foils. Fracture and Structural Integrity, 11(42), pp. 328-336. DOI: https://doi.org/10.3221/IGF-ESIS.42.34.

[6] Fu, M. W., Chan, W. L. (2013). A review on the state-of-the-art micro forming technologies. The International Journal of Advanced Manufacturing Technology, 67(9), pp. 2411-2437. DOI: https://doi.org/10.1007/s00170-012-4661-7.

[7] Fu, M. W., Chan, W. L. (2011). Geometry and grain size effects on the fracture behavior of sheet metal in micro-scale plastic deformation. Materials & Design, 32(10), pp. 4738-4746. DOI: https://doi.org/10.1016/j.matdes.2011.06.039.

[8] Meng, B., Wang, W. H., Zhang, Y. Y., Wan, M. (2019). Size effect on plastic anisotropy in microscale deformation of metal foil. Journal of Materials Processing Technology, 271, pp. 46-61. DOI: https://doi.org/10.1016/j.jmatprotec.2019.03.023.

[9] Xu, J., Guo, B., Shan, D., Li, M., Wang, Z. (2013). Specimen dimension and grain size effects on deformation behavior in micro tensile of SUS304 stainless steel foil. Materials Transactions, 54(6), pp. 984-989. DOI: https://doi.org/10.2320/matertrans.M2013016.

[10] Simons, G., Weippert, C., Dual, J. and Villain, J. (2006). Size effects in tensile testing of thin cold rolled and annealed Cu foils. Materials Science and Engineering: A, 416(1-2), pp. 290-299. DOI: https://doi.org/10.1016/j.msea.2005.10.060.

[11] Klein, M., Hadrboletz, A., Weiss, B., Khatibi, G. (2001). The 'size effect'on the stress–strain, fatigue and fracture properties of thin metallic foils. Materials Science and Engineering: A, 319, pp. 924-928. DOI: https://doi.org/10.1016/S0921-5093(01)01043-7.

[12] Meng, B., Zhang, Y. Y., Cheng, C., Han, J. Q., Wan, M. (2018). Effect of plastic anisotropy on microscale ductile fracture and microformability of stainless steel foil. International Journal of Mechanical Sciences, 148, pp. 620-635. DOI: https://doi.org/10.1016/j.ijmecsci.2018.09.027.

[13] Weiss, M., Zhang, P., Pereira, M. P., Rolfe, B. F., Wilkosz, D. E., Hodgson, P. D. (2020). Understanding size effects and forming limits in the micro-stamping of industrial stainless steel foils. Metals, 11(1), 38. DOI: https://doi.org/10.3390/met11010038.

[14] Duan, X., Saxena, K. K., Wang, J., Arshad, M. H., Ayesta, I., Wang, Y., Reynaerts, D., Yang, X. (2025). Residual stress and its modification strategies in the surface/sub-surface layer of components machined by electrical discharge machining: a review. The International Journal of Advanced Manufacturing Technology, 139, pp. 41–58. DOI: https://doi.org/10.1007/s00170-025-15861-9.

[15] Abu Qudeiri, J. E., Saleh, A., Ziout, A., Mourad, A. H. I., Abidi, M. H., Elkaseer, A. (2019). Advanced electric discharge machining of stainless steels: Assessment of the state of the art, gaps and future prospect. Materials, 12(6), 907. DOI: https://doi.org/10.3390/ma12060907.

[16] Kwame, J. S., Yakushina, E., Blackwell, P. (2020). Impact of machining-induced surface defects on the edge formability of commercially pure titanium sheet at room temperature. SN Applied Sciences, 2(12), 1999. DOI: https://doi.org/10.1007/s42452-020-03839-z.

[17] Feistle, M., Kindsmüller, A., Pätzold, I., Golle, R., Volk, W. (2022). Influence of sheet metal pre-forming on edge crack sensitivity using an AHSS steel grade. International Journal of Material Forming, 15(4), 50. DOI: https://doi.org/10.1007/s12289-022-01669-5.

[18] Krolczyk, G., Legutko, S., Nieslony, P., Gajek, M. (2014). Study of the surface integrity microhardness of austenitic stainless steel after turning. Tehnički vjesnik, 21(6), pp. 1307-1311.

[19] Pham, C. H., Thuillier, S., Manach, P. Y. (2015). Mechanical properties involved in the micro-forming of ultra-thin stainless steel sheets. Metallurgical and Materials Transactions A, 46(8), pp. 3502-3515. DOI: https://doi.org/10.1007/s11661-015-2978-1.

[20] Kar, S., Kulkarni, S. D. (2026). Surface texturing through photochemical machining for enhanced tribological performance: a review. Journal of Tribology, 148(2), 020803.
[21] Zhang, G. P., Takashima, K., Higo, Y. (2006). Fatigue strength of small-scale type 304 stainless steel thin films. Materials Science and Engineering: A, 426(1-2), pp. 95-100. DOI: https://doi.org/10.1016/j.msea.2006.03.090.
[22] Song, D., Wu, W. (2024). Study on Electrical and Mechanical Properties of Double-End Supported Elastic Substrate Prepared by Wet Etching Process. Micromachines, 15(7), 929. DOI: https://doi.org/10.3390/mi15070929.
[23] Velterop, L. (2003). Influence of wire electrical discharge machining on the fatigue properties of high strength stainless steel. NLR-TP-2003-104.
[24] Zhou, Y. (2025). Effect of milling parameters on the surface integrity and corrosion behaviour of austenitic stainless steel. Matéria (Rio de Janeiro), 30, e20250131. DOI: https://doi.org/10.1590/1517-7076-RMAT-2025-0131.
[25] Qian, L., Ji, W., Sun, C., Fang, G., Lian, J. (2021). Prediction of edge fracture during hole-flanging of advanced high-strength steel considering blanking pre-damage. Engineering Fracture Mechanics, 248, 107721. DOI: https://doi.org/10.1016/j.engfracmech.2021.107721.
[26] Mateo, A., Fargas, G., Calvo, J., Roa, J. J. (2015). Influence of laser cutting on the fatigue limit of two high strength steels. Materials Testing, 57(2), 136-140. DOI: https://doi.org/10.3139/120.110686.
[27] Buglioni, L., Krahmer, D. M., Sánchez Egea, A. and Simoncelli, A. (2025). Implications of stress concentrators and work hardening in flat tensile samples subjected to milling and abrasive water jet machining. The International Journal of Advanced Manufacturing Technology, 136(1), pp. 343-351. DOI: https://doi.org/10.1007/s00170-024-14118-1.
[28] Feistle, M., Kindsmüller, A., Pätzold, I., Golle, R., Volk, W. (2022). Influence of sheet metal pre-forming on edge crack sensitivity using an AHSS steel grade. International Journal of Material Forming, 15(4), 50. DOI: https://doi.org/10.1007/s12289-022-01669-5.
[29] Blaber, J., Adair, B., Antoniou, A. (2015). Ncorr: open-source 2D digital image correlation matlab software. Experimental Mechanics, 55(6), pp. 1105-1122. DOI: https://doi.org/10.1016/S0921-5093(01)01043-7
[30] Tong, W., Yao, H., Xuan, Y. (2011). An improved error evaluation in one-dimensional deformation measurements by linear digital image correlation, Experimental Mechanics, 51(9), pp. 1019–1031. DOI: https://doi.org/10.1007/s11340-010-9423-6.
[31] Meng, B., Wang, W. H., Zhang, Y. Y., Wan, M. (2019). Size effect on plastic anisotropy in microscale deformation of metal foil. Journal of Materials Processing Technology, 271, pp. 46-61. DOI: https://doi.org/10.1016/j.jmatprotec.2019.03.023.
[32] Lai, X., Peng, L., Hu, P., Lan, S., Ni, J. (2008). Material behavior modelling in micro/mesoscale forming process with considering size/scale effects. Computational Materials Science, 43, pp. 1003–1009. DOI: https://doi.org/10.1016/j.commatsci. 2008.02.017.
[33] Goshert, B., Terrazas, O. R., Matlock, D. K., Van Tyne, C. J. (2018). Sample edge effects on tensile properties and sheet formability. In IOP Conference Series: Materials Science and Engineering, 418(1), 012064. DOI: https://doi.org/10.1088/1757-899X/418/1/012064.
[34] Chen, C. H., Lee, R. S., Gau, J. T. (2010). Size effect and forming-limit strain prediction for microscale sheet metal forming of stainless steel 304. The Journal of Strain Analysis for Engineering Design, 45(4), pp. 283-299. DOI: https://doi.org/10.1243/03093247JSA.
[35] Weiss, M., Zhang, P., Pereira, M. P., Rolfe, B. F., Wilkosz, D. E., Hodgson, P. D. (2020). Understanding size effects and forming limits in the micro-stamping of industrial stainless steel foils. Metals, 11(1), 38. DOI: https://doi.org/10.3390/met11010038.